THE EFFECT OF RAREFACTION LEVEL ON SHOCK/SHOCK INTERFERENCES APPLIED TO ATMOSPHERIC RE-ENTRY: EXPERIMENTAL STUDY IN A SUPERSONIC RAREFIED FLOW

Vincente Cardona, Viviana Lago

THE EFFECT OF RAREFACTION LEVEL ON SHOCK/SHOCK INTERFERENCES APPLIED TO ATMOSPHERIC RE-ENTRY: EXPERIMENTAL STUDY IN A SUPERSONIC RAREFIED FLOW

Vincente Cardona, Viviana Lago

CNRS, ICARE, UPR 3021,
1c av. de la Recherche Scientifique, CS 50060, F-45071, Orléans cedex 2, France

ABSTRACT

In the case of proximal bodies flying in Earth's atmosphere, shock/shock interferences can occur. According the altitude, interacting bodies suffer different rarefaction levels which impact their aerodynamics and trajectories. To better understand the effect of rarefaction level, the six types of shock/shock interferences were studied with two iso-Mach number nozzles of the MARHy wind tunnel with different Reynolds and Knudsen numbers: M4 - 2.67 Pa and M4 - 8 Pa nozzles. Models used for the experiments are a couple of spheres of same diameter, representative of 1-m diameter blunt bodies interacting at 76 and 69 km in altitude. Results are obtained with three different diagnostics allowing to explore the influence of the viscosity on shock wave interferences. They enlighten differences in terms of shock wave shapes, pressure distribution on the following sphere, and values of forces and wall pressures.

Index Terms— Aerodynamics, Atmospheric re-entry, Supersonic rarefied flow, Shock/shock interferences, Wind tunnel

1. INTRODUCTION

The studies of proximal bodies flying in Earth's atmosphere can be associated to a multitude of applications whether in the case of a spacecraft launch or the re-entry of space debris. In the case of spacecraft launch, shock/shock interferences (SSI) of a Two-Stage-To-Orbit were studied to propose a new booster model that enable lower heat transfer rate [1][2], or to better understand the stage separation [3] that occurs at 70 to 90 km. In the case of space debris or meteoroid re-entry, the fragmentation occurring around 80 km in altitude also results in SSI.

Proximal bodies interaction have often been studied [4]. Most of these studies were conducted in the continuum regime, numerically by using Computational Fluid Dynamic (CFD) and experimentally. However, as the flight altitude increases, the rarefaction level impacts the aerodynamics due to viscous effects. Some numerical studies took into account rarefaction effects [5], but few are those who experimented SSI in a rarefied flow [6].

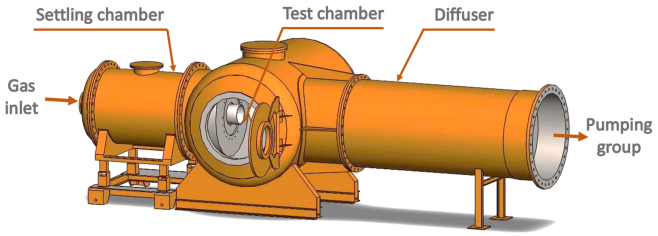

Fig. 1. MARHy wind tunnel

The present study proposes to better understand the effect of the rarefaction level on SSI occuring at high altitudes. This work is focused on the interaction of bow shock waves produced by two spheres at two different levels of rarefaction but same velocity. Results will help deepen the physics of SSI in a rarefied flow, and will serve as a database for the completion of numerical method.

2. EXPERIMENTAL SETUP

2.1. Test facility

The experiments were carried out in the MARHy wind tunnel (Fig. 1), at ICARE, CNRS, Orléans. MARHy is a low density facility that produces flows with Mach numbers from 0.8 to 20 thanks to a large set of nozzles. The powerful pumping group, composed with 16 pumps, allows to obtain steady operating conditions with no limit in time. Regardless the nozzle used, the flow is laminar and homogeneous in the isotropic core (which diameter and length vary according the nozzle used). For this study, the M4 - 2.67 Pa (Nozzle a) and M4 - 8 Pa (Nozzle b) nozzles presented in Table 1 were used to investigate the impact of the rarefaction level on shock/shock interferences. The stagnation conditions (subscript $_o$) refer to the settling chamber, and the free-stream conditions (subscript $_\infty$) are those in the test chamber. The two chambers are separated by a nozzle which imposes flow conditions in terms of free-stream pressure and Mach number, due to its specific design.

Table 1. Flow conditions in the MARHy wind tunnel for Nozzle a (M4 - 2.67 Pa) and Nozzle b (M4 - 8 Pa)

		Nozzle a	Nozzle b
Stagnation conditions			
gas		ambient air	ambient air
p_o	(Pa)	404.79	1214.39
Te_o	(K)	293.15	293.15
ρ_o	(kg.m^{-3})	4.81×10^{-3}	1.44×10^{-2}
Free-stream conditions			
gas		ambient air	ambient air
p_∞	(Pa)	2.67	8.00
Te_∞	(K)	69.80	69.80
ρ_∞	(kg.m^{-3})	1.33×10^{-4}	3.99×10^{-4}
μ_∞	(Pa.s)	4.84×10^{-6}	4.84×10^{-6}
U_∞	(m.s^{-1})	669.92	669.92
Re_{u_∞}	(m^{-1})	1.84×10^{4}	5.52×10^{-4}
Ma_∞		4	4
λ_∞	(m)	2.23×10^{-4}	7.40×10^{-5}

The free-stream Mach number only depends on the stagnation and free-stream pressures. The stagnation pressure is accurately regulated with the opening of a micro-valve at the gas inlet. The free-stream pressure is set by commissioning the needed number of pumps, and then regulated by adjusting the opening of a butterfly valve placed between the diffuser and the pumping group. The stagnation and free-stream pressures are respectively monitored with a 10 Torr and a 0.1 Torr MKS absolute pressure sensors accurate at 0.15% and 0.12% of reading.

2.2. Models

As for many studies on proximal bodies, the experimented models are spheres. The two spheres are equal in size (16 mm in diameter) and are made of polyoxymethylene (POM). They are covered with a thin layer of black spray paint for visual reasons.
The Tsien number (1), also called the viscous parameter, is a dynamic similitude parameter that includes velocity and viscosity effects.

$$\sigma = \frac{Ma_\infty}{\sqrt{Re_\infty}} \tag{1}$$

It enables to characterize rarefaction level and determine the altitude experimentally simulated. Prévereaud *et.al* [7] calculated the velocity of a 1 m-diameter sphere, at different altitudes. By analogy, a 16-mm sphere flying in the free-stream conditions detailed in Table 1 is representative of a 1-m blunt body flying at 76 km for Nozzle a, and 69 km for Nozzle b. The Knudsen numbers are respectively 1.39×10^{-2} and 4.64×10^{-3}, representatives of slip regime.

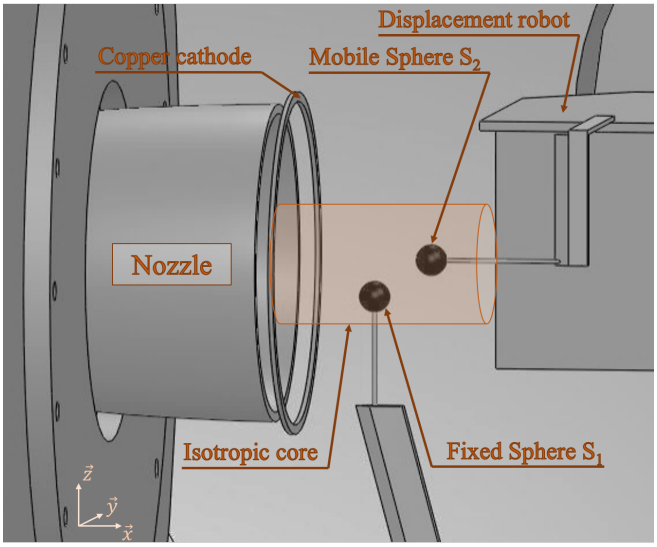

Fig. 2. Models and their placement in the isotropic core

2.3. General set-up and experimental devices

In order to study the effect of rarefaction level on the SSI, three types of measurement were realized. The glow discharge technique enables to visualize shock-waves, and two quantitative measurements gave the drag and lift forces (measured with an aerodynamic balance), and the wall pressures (measured with a differential pressure sensor). The general set-up and the measurement techniques will be explained in the following sections.

2.3.1. General set-up

Figure 2 shows the general experimental set-up used. The first sphere (S_1) is fixed and held by a vertical profiled support mounted on a pneumatic rotary actuator that enables to remove S_1 from the flow. The other sphere (S_2) is held by the rear with an adapted profiled support mounted on a tri-axial displacement robot so that S_2 can be displaced behind S_1. Both spheres are placed in the middle plane of the isotropic core in the $\vec{y}$-direction. The diameter of the core is 7.5 cm for Nozzle a and 8 cm for Nozzle b. Due to the small diameter of the nozzles S_1 is placed below the horizontal plane of the nozzle, in order to enlarge the displacement area of S_2. The placement of S_1 in the isotropic core does not impact much its shock-wave, as explained in a previous work [8]. S_2 is placed 24 mm behind S_1 is the $\vec{x}$-direction, and its altitude (in the $\vec{z}$-direction) varies to obtain the different types of SSI.

2.3.2. Glow-discharge technique

The visualization of the flow field is the first step that enables to determine the positions of the six types of SSI. In a rarefied flow, the density is so low that no optical technique based on

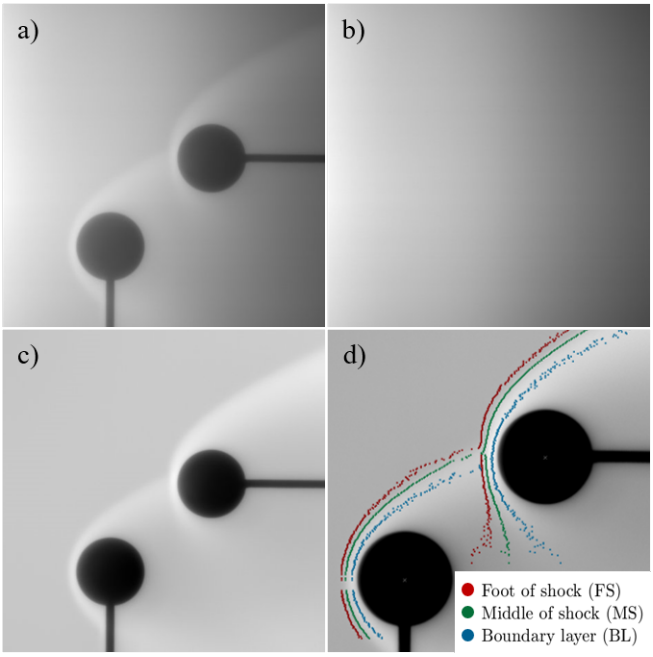

Fig. 3. Image post-processing. a) average image with models, b) average image without models, c) normalized image, and d) normalized image with shock wave detection.

index variation can be applied successfully.
As seen in Fig. 2, a copper ring cathode is placed around the isotropic core, at the exit of the nozzle. A negative voltage of -1 to -1.20 kV is applied on the cathode, ionizing particles. This technique is called the glow-discharge and allows to illuminate rarefied flows: the denser the flow, the greater the light intensity.
Using a Kuro CMOS camera equipped with a VUV objective lens, a set of 200 images were recorded for each position of S_2 towards S_1. Another set of 200 images were recorded for the visualization of the flow without models. In Fig. 3 are presented the mean images of the recordings with and without models (see a) and b)). Images are averaged to reduce the noise of raw images. This method can be applied thanks to the steady continuous flow in the test chamber.
In order to avoid the luminous gradient due to the source of ionization, the averaged image with model a) was divided by the background image b), giving the normalized image c) which does not present luminous gradient and makes it possible to auto-detect shock waves. Image d) shows the normalized image with the shock waves detected thanks to the Fourier self-deconvolution method detailed by Kovacs *et.al* [9]. In rarefied flows, the shock waves are thick and, as can be seen in image d), they are described by three regions: the foot of shock (FS), the middle of shock (MS) and the boundary layer (BL). More details concerning these regions and their location are presented in the works of Kovacs *et.al* [9], and of Cardona *et.al* [8].

2.3.3. Aerodynamic balance

The aerodynamic balance used for the measurement of drag and lift forces was designed, tested and experimented by Noubel and Lago [10]. This device was also confronted to a pendulum method [11] that allows to measure drag forces, and the results of the two methods showed a good agreement. The balance is composed of two modules made of thin slates that deform according the perceived forces. The slats are equipped with strain gauges that send an electrical signal previously calibrated to allow its conversion into a force. The slats need to be positioned perpendicularly to the vertical axis ($\vec{z}$) not to suffer gravity forces. Consequently, the balance measures the drag force in the $\vec{x}$-direction, and lift force in the $\vec{y}$-direction. So, contrarily to the set-up used for the visualization of shock waves, the axis of displacement of S_2 will not be vertical (in the $\vec{z}$-direction), but transversal (in the $\vec{y}$-direction). As a consequence, S_1 and S_2 are in the horizontal plane of the core middle, and S_1 is displaced in the $-\vec{y}$-direction to ensure a sufficiently large area of displacement for S_2. This does not change the flow seen by S_2 while the two spheres are contained in the core since it is isotropic.
As shown in Fig. 4, two measurements are realized. One measurement records, during 10 s, the forces perceived by S_2 behind S_1 (see the top image). As the pumping group constantly vacuum the test chamber, the measured forces correspond to the forces from the flow (the one perceived naturally by S_2) plus the suction forces from the pumping group. In order to remove suction forces from the measured values, an other measurement is recorded during 10 s, this time with a plate in front of S_2 (see the bottom image), so that S_2 and the balance do not see any force from the flow. The drag and lift forces are calculated by averaging each set and subtracting the suction forces from the global forces perceived by S_2. For the accuracy of the measurements, these two recordings are realized ten times. Drag and lift forces are given with an accuracy of 0.1 mN.

2.3.4. Wall pressure measurement

For the wall pressure measurement, the general configuration and the sphere placement are the same as for the visualization (S_2 moves in the $\vec{z}$-direction).
Figure 5 shows the wall pressure set-up viewed from the side (top schemes) and from the top (bottom schemes). S_2 is drilled in two directions: in the $\vec{x}$-direction, the hole is 1.2 mm-diameter and serves as entrance for the air molecules; in the $\vec{y}$-direction, the 3 mm-diameter hole serves for the maintaining of S_2 (a tube is hermetically inserted in it), for its rotation (the tube is placed in a rotary system placed on the displacement robot), and for connection to the pressure sensor (via a flexible hose). Consequently, S_2 can be displaced behind S_2, and rotated about the $\vec{y}$-direction. The pressure at its surface can be measured on the vertical line of the sphere for different types of SSI.

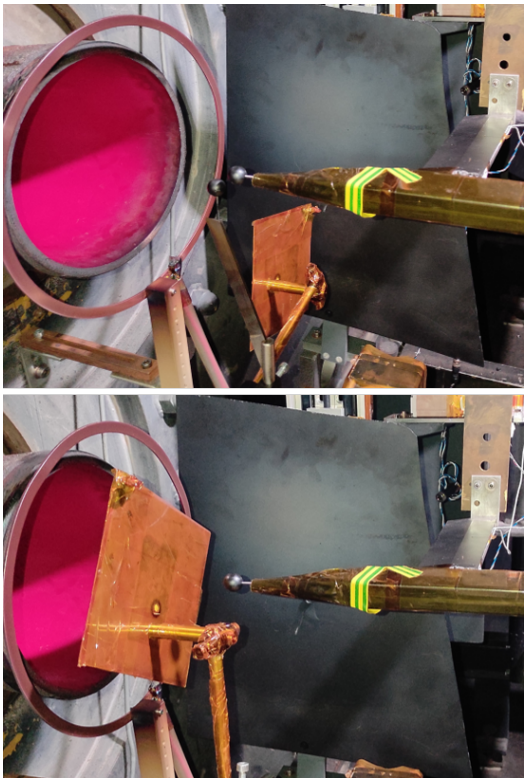

Fig. 4. Set-up of the aerodynamic balance. Top image: Measurement of the forces applied on the sphere. Bottom image: Measurement of the suction forces of the roots blowers

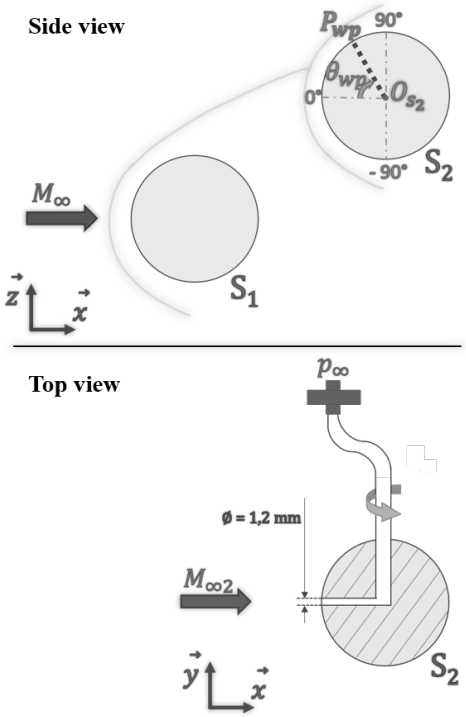

Fig. 5. Schematics of the set-up of the wall pressure measurement - side view (top schemes) and top view (bottom schemes).

The used pressure sensors are differential Validyne DP103 that can measure very low pressures up to 0.0125 psi for Nozzle a (86 Pa with 0.43 Pa accuracy), and 0.02 psi for Nozzle b (138 Pa with 0.69 Pa accuracy). A differential pressure sensor is made of two cavities separated by a sensitive deforming membrane. In order not to deform this membrane with gravity or vibrations, the pressure sensors are placed vertically on a vibration absorbing support. On one side of the membrane, the pressure is that at the surface of the sphere, and on the other side, the pressure is the free-stream pressure. Since the free-stream pressure is monitored by an MKS absolute pressure as already described, it is known. In consequence the wall pressure can be calculated by subtracting free-stream pressure from the measured pressure. The two sensors were calibrated on and beyond their own range and showed a linear deformation of the membrane until 150 Pa for the 0.0125 psi, and 350 Pa for the 0.02 psi, which includes our measured values.

For each position of S_2 towards S_1, the wall pressure is measured for angles from 90° to -90°. At the end of each position (-90°), S_2 is rotated to its initial angle (90°) where a second measurement is realized to verify the accuracy of measurements.

3. RESULTS AND DISCUSSION

In this section, the two experimental conditions are compared using the results of the three types of measurement.

3.1. Shock/shock interferences

The shock/shock interferences were first analyzed qualitatively thanks to the shock wave detection. In order to compare the two experimented flow conditions, the middles of shock wave were superposed for each type of SSI as shown in Fig. 6, where plots are zoomed on the interference area. Whatever the type of SSI, three features can be observed:

- In both cases (Nozzle a and Nozzle b) the same patterns of shock/shock interference are observed:
  - For SSI types I to III, there is a flattening of the shock wave below the intersection point.
  - For SSI types V and VI, there is a flattening of the shock wave above the intersection point.
  - For SSI types I and IV, there is a step-back area of the shock wave at the intersection point.
  - From type I to VI, the lower part of the shock wave (below P_i, the point of intersection between S_1 and S_2 middles of shock) progressively opens.

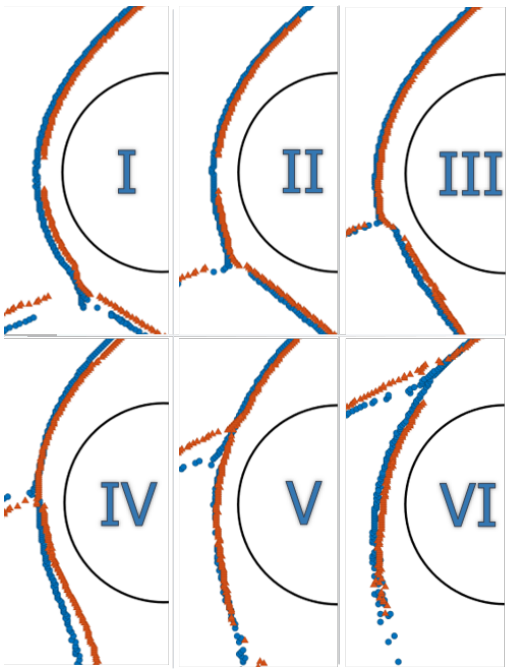

Fig. 6. Superposition of shock waves obtained with Nozzle a (blue circle) and Nozzle b (orange triangle) for each type of shock/shock interference.

A wider explanation is given in Cardona *et.al* [8].

- Whether S_2 is globally in the free-stream or globally in the wake of S_1, the global level of rarefaction is lower for Nozzle a than for Nozzle b. As the level of rarefaction decreases, the middle of shock wave gets closer to the surface of S_2. This result is in accordance with the work of Rembaut *et.al* [12] who experimentally demonstrated that the stand-off distance of a sphere in a free-stream flow decreases with the decrease of the Knudsen number.

- As the level of rarefaction decreases, the specificities of SSI are slightly accentuated, mostly for SSI types I to IV. Note that differences are not much pronounced because the levels of rarefaction of the two nozzles are close. Nevertheless, this phenomenon is due to a global increase in pressure values and to less diffuse shock waves, leading to a stronger impact between the shock waves.

Another feature concerns the thickness of the shock wave. Figure 7 presents the superposition of Nozzle a and Nozzle b shock waves in the intersection area for the three shock regions of the type III SSI. As can be observed, the boundary layers of the two cases are superposed, while the distance between Nozzle a and Nozzle b shock waves increases for the middles of shock and further more for the foots of shock. This means that the shock becomes thicker with a higher Knudsen number. Here, only the type III SSI is presented, but same results are observed for the five other types.

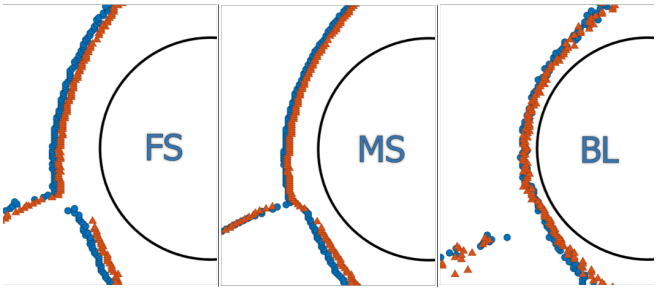

Fig. 7. Superposition of the foots of shock (FS), middles of shock (MS) and boundary layers (BL) obtained with Nozzle a (blue circle) and Nozzle b (orange triangle) for the type III shock/shock interference.

3.2. Drag and lift forces

For each type of SSI, one position of S_2 towards S_1 was chosen for the measurement of the aerodynamic forces of S_2. Figure 8 presents drag (F_x) and lift (F_z) forces of S_2 plotted according Θ_i, the angle that makes the segment $[P_i\ O_{S_2}]$ with the horizontal, where P_i is the point of intersection between S_1 and S_2 middles of shock and O_{S_2} is the center of the sphere S_2.

Drag force values are divided by F_{x_0}, the force of S_2 alone in the free-stream, in order to highlight the impact of the type of SSI on the drag force of S_2. Respectively for Nozzle a and Nozzle b, $(F_{x_0})_a = 8.1$ mN and $(F_{x_0})_b = 21.5$ mN. As can be seen, the dimensionless drag forces (F_{x_d}) of the Nozzle a and Nozzle b are equals for SSI types I, II and half of III. Then the slopes separate: for Nozzle b, F_{x_d} reaches a maximum for the SSI type III and decreases slowly until type V SSI, then decreases a bit faster; while for Nozzle a, F_{x_d} keep increasing until type IV SSI, and then decreases. This graph shows that the type of SSI where the drag force is maximal depends on the rarefaction level. Also, as the rarefaction level decreases, the impact of types IV and V SSI seems to diminish. Indeed, with lower local rarefaction, shock waves are denser but thinner. At P_i, the intersection point, the incident shock begins to penetrates the boundary layer of S_2, but more locally than for Nozzle a. It is possible that the impacted area at the surface of S_2 is small enough to induce a decrease in drag forces, even if parietal forces are locally higher.

The lift force values are not divided by the reference force because a single sphere has a null lift force. Nevertheless, it can be seen that the maximal value is reached for a type III SSI for Nozzle a while it is reached for a type II SSI for Nozzle b. Moreover, it seems that the lift force is positive for a wider range of S_2 positions when the rarefaction level increases.

F_{x_0} and F_{z_0} are representative of the drag and lift forces of S_1. Consequently, with the value of S_2 drag and lift forces,

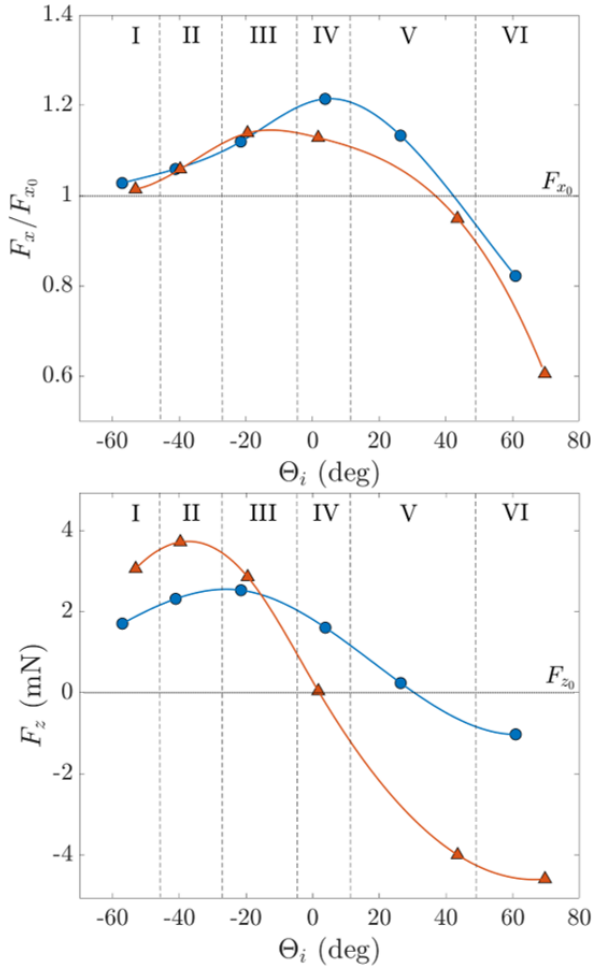

Fig. 8. Dimensionless drag force (top graph) and lift force (bottom graph) according the interaction angle obtained with Nozzle a (blue circle) and Nozzle b (orange triangle).

the displacement of S_2 in S_1 reference frame can locally be deduced:

- if $F_x < F_{x_0}$, S_2 approaches S_1 horizontally ($\Leftarrow$)
- if $F_x > F_{x_0}$, S_2 moves away from S_1 horizontally ($\Rightarrow$)
- if $F_z < F_{z_0}$, S_2 approaches S_1 vertically ($\Downarrow$)
- if $F_z > F_{z_0}$, S_2 moves away from S_1 vertically ($\Uparrow$)

By combining the vector of the drag force with this of the lift force, the resulting force of S_2 (calculated in S_1 spatial referential) gives the local displacement of S_2 towards S_1, as shown by the arrows in Fig. 9. For Nozzle a, S_2 is more repulsed by the wake of S_1 than for Nozzle b for which it is clearly seen that for types V and VI SSI, S_2 is strongly attracted by S_1. For Nozzle b, this attraction can be the consequence of a denser S_1 shock wave that prevents S_2 to go through the incident shock, and potentially makes S_2 ricocheting on it.

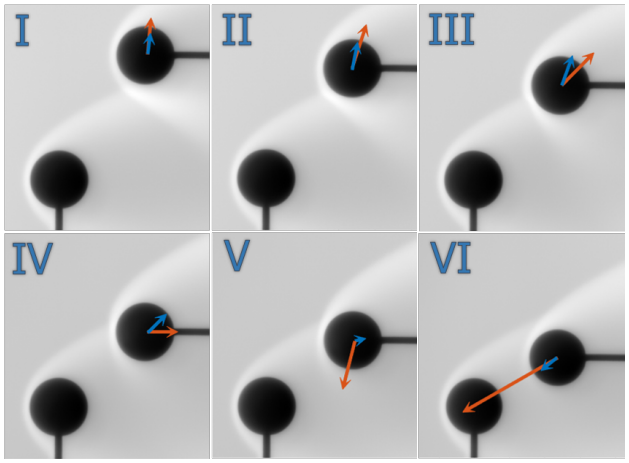

Fig. 9. Calculated displacement of S_2 in S_1 reference frame according the shock/shock interaction type for Nozzle a (blue arrow) and Nozzle b (orange arrow).

3.3. Wall pressure

The pressure at the surface of S_2 were recorded for the same positions than those adopted for the measurement of aerodynamic forces. For each type of SSI, Fig. 10 gives the pressure distribution according Θ_{wp}, the angle that makes the segment $[P_{wp}\ O_{S_2}]$ with the horizontal, where P_{wp} is the point of the pressure measurement at the surface of S_2 and O_{S_2} is the center of the sphere S_2, as described in 5. Concerning Θ_{wp}, -90° represents the bottom of S_2, and 90° its top. Wall pressure are normalized with p_{w_0}, the wall pressure at the stagnation point of a single sphere in the free-stream. Respectively for Nozzle a and Nozzle b, $(p_{w_0})_a = 54.17$ Pa and $(p_{w_0})_b = 164.04$ Pa. The given data is dimensionless so that the analysis only highlights shock/shock interferences differences according the nozzle used, this way, only the effect of rarefaction is shown.

As can be seen, for each type of SSI, a specific pattern appears, and it is the same for the two nozzles. For the SSI types I, II and III, only the part below the intersection area sees a variation of wall pressure. As S_2 is manly outside of S_1 wake, the region above the intersection area is still in the free-stream so the upper surface of S_2 presents the same pressure distribution than for the reference case. For these first three types, in particular for the types I and III, it seems that wall pressure variation are more emphasized for Nozzle b. As this phenomenon is more marked for the type IV SSI, it will be explained in the next paragraph.

For SSI type IV, the evolution of the curve presents three slopes. For Nozzle b, a first set of wall pressure were recorded (empty triangle), but as the pressure peak was not at the same angle than for Nozzle a, another set were recorded (solid triangle). As the measurements of wall pressure are time consuming, the second recording was only made around the pres-

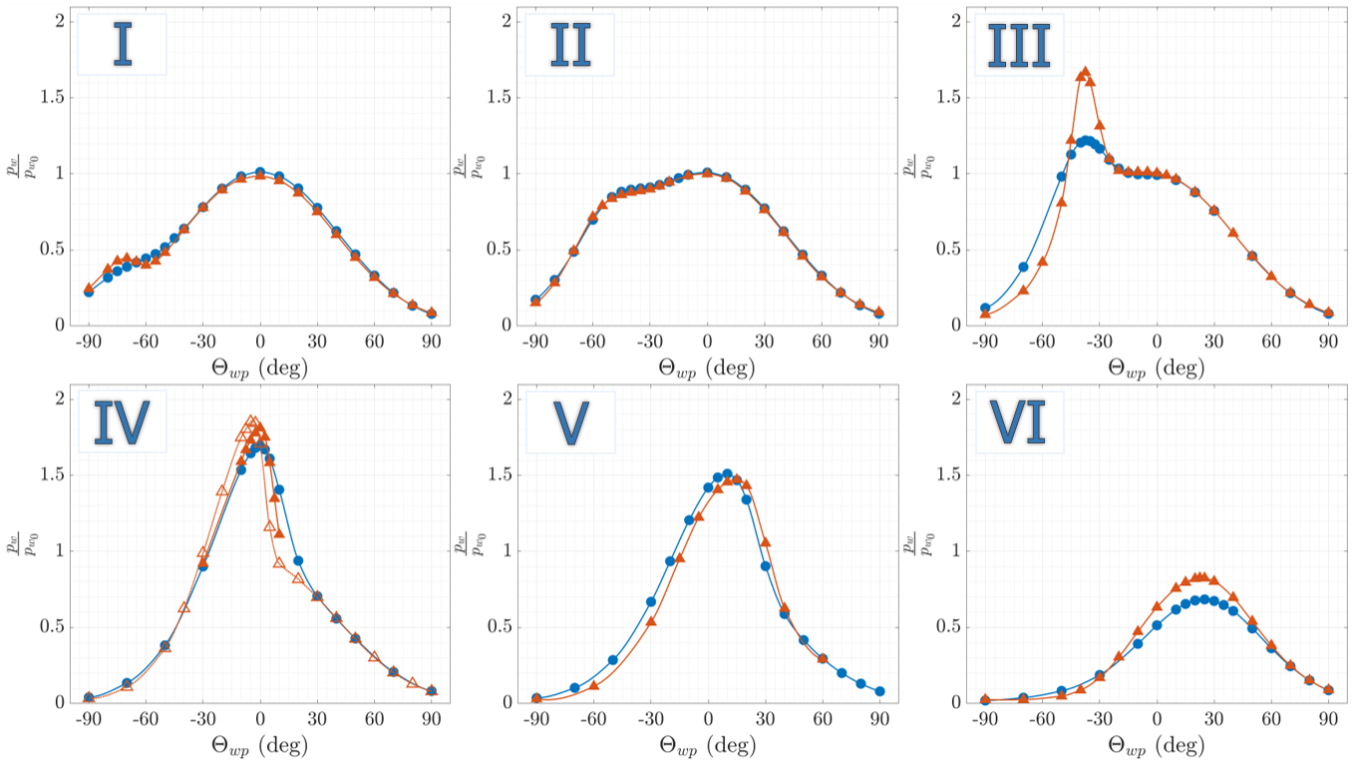

Fig. 10. Pressure distribution for the six types of shock/shock interferences for Nozzle a (blue circle) and Nozzle b (orange triangle).

sure peak. It enables to observe that for the exact same position of pressure peak, the wall pressure of the two flow conditions present a slight difference in terms of distribution in the interference area. For Nozzle b, there is a pronounced inflection around 10°, where the incident shock wave probably does interfere with S_2 shock wave anymore. As the level of rarefaction increases, shock waves get thicker and the interference area is smoother and bigger. In consequence, as the incident shock wave penetrates S_2 shock wave it diffuses in its boundary layer, and so the wall pressures are a bit lower at the peak but the impacted region is bigger.

For the types V and VI, there is not much of a difference between both rarefaction level. S_2 being mainly in the wake of S_1, the local rarefaction level is higher than in the free-stream, which results in a global decrease of the pressure values. Moreover, the interaction between the two shock waves is located at the top of S_2 or even higher, so its surface is not directly impacted, but the flow around it is. This results in an absence of pressure peak in a deformed area as observed for the other types of interference.

Fig. 11 shows the values of maximal pressure in the interference area, where the deformation of the slopes are observed, according the angle of interference. It shows that whatever the SSI type, pressure peaks are greater for the least rarefied flow. Fig. 12 presents the area under the pressure curves (AUPC) presented in Fig. 10 according the angle of interference. The AUPC is representative of the pressure forces exercised at the front line of S_2. As can be observed looking at the types III and IV, values are slightly higher for Nozzle a, where the flow is the most rarefied and the shock waves are thicker. From Fig. 11 and Fig. 12, it can be assumed that with an increase in rarefaction level, the lower pressure peaks are compensated by the fact that the pressure is distributed more widely over the surface of S_2.

4. CONCLUSION

Trough the different experiments carried out in the MARHy wind tunnel, the impact of shock/shock interferences was studied for two levels of rarefaction.

The analysis of the flow field images enabled to detect shock waves and, in particular, the different patterns of the six types of SSI. For the two experimented conditions, the SSI patterns are similar but two features were noticed: an increase of the rarefaction level results in the increase of the shock waves thickness, leading to a larger interference area and to a less pronounced pattern.

The measurements of drag and lift forces showed that the maximal forces do not occur for the same interference angle and thus for different types of SSI. The maximal drag and lift

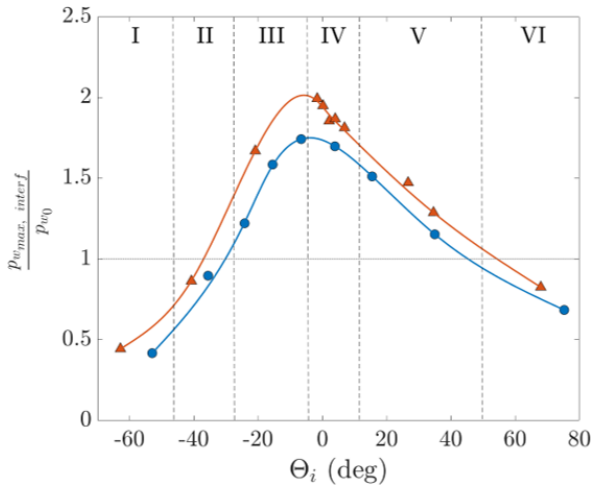

Fig. 11. Dimensionless pressure peak in the interference area according the interaction angle for Nozzle a (blue circle) and Nozzle b (orange triangle).

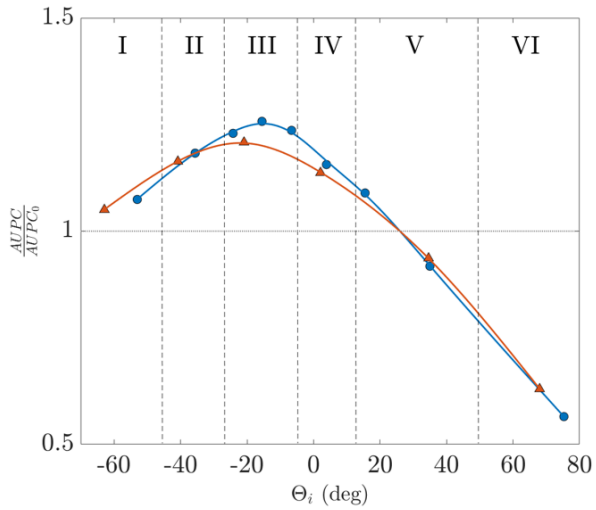

Fig. 12. Dimensionless area under pressure curve (AUPC) according the interaction angle for Nozzle a (blue circle) and Nozzle b (orange triangle).

forces are respectively obtained for SSI types IV and III for the highest rarefaction level and are higher than for the other experimental conditions, for which maximums are obtained for SSI types III and II.

Observing wall pressure results, an increase of the rarefaction level also tends to show less pronounced SSI. The distribution of maximal wall pressure according the angle of interaction shows that a lower level of rarefaction implies higher pressure peak. The area under pressure curves shows the same results than the drag forces.

Globally, interferences are less pronounced, and pressure peaks are lower for a higher rarefaction level. But the larger distribution of forces generate a greater impact of SSI for types III and IV.

5. REFERENCES

[1] K Hanai, H Ozawa, and Y Nakamura, "Two-stage-to-orbit booster configuration for reducing aerodynamic heating at hypersonic speed," in *37th AIAA Fluid Dynamics Conference and Exhibit*, 2007, p. 4220.

[2] J Jia, D Fu, and Z He, "Aerodynamic interactions of a reusable launch vehicle model with different nose configurations," *Acta Astronautica*, vol. 177, pp. 58–65, 2020.

[3] W Bordelon, A Frost, and D Reed, "Stage separation wind tunnel tests of a generic tsto launch vehicle," in *21st AIAA Applied Aerodynamics Conference*, 2013, p. 4227.

[4] S J Laurence, R Deiterding, and G Hornung, "Proximal bodies in hypersonic flow," *Journal of Fluid Mechanics*, vol. 590, pp. 209–237, 2007.

[5] C White and K Kontis, "The effect of increasing rarefaction on the edney type iv shock interaction problem," in *International Conference on RailNewcastel Talks*. 2018, pp. 299–311, Springer, Cham.

[6] V V Riabov and A V Botin, "Shock interference in hypersonic rarefied-gas flows near a cylinder," in *17th Applied Aerodynamics Conference*, 1999, p. 3207.

[7] Y Prevereaud, J L Vérant, J M Moschetta, F Sourgen, and M Blanchard, "Debris aerodynamic interactions during uncontrolled atmospheric reentry," in *AIAA Atmospheric Flight Mechanics Conference*, 2012, p. 4582.

[8] V Cardona, R Joussot, and V Lago, "Shock/shock interferences in a supersonic rarefied flow: experimental investigation," *Experiments in Fluids*, vol. 62, no. 6, pp. 1–14, 2021.

[9] L Kovacs, P-Y Passaggia N, Mazellier, and V Lago, "Detection method for shock-waves in viscous flows," *Experiments in Fluids*, vol. 63, no. 1, pp. 1–16, 2022.

[10] H Noubel and V Lago, "Experimental analysis of waverider lift-to-drag ratio measurements in rarefied and supersonic regime," 2021.

[11] V Cardona and V Lago, "Aerodynamic forces of interacting spheres representative of space debris re-entry: Experiments in a supersonic rarefied wind-tunnel," *Acta Astronautica*, 2021.

[12] N Rembaut, R Joussot, and V Lago, "Aerodynamical behavior of spherical debris in the supersonic and rarefied wind tunnel marhy," *Journal of Space Safety Engineering*, vol. 7, no. 3, pp. 411–419, 2020.